Development of an anti-reflection coating for optical windows in multimode electro-optical detection systems

HUI Bing, LIU Nan-nan, PENG Yong-chao, FU Xiu-hua, BAI Yue-jie, YANG Lu-yan, DONG Suo-tao, JIA Feng

Citation:
HUI Bing, LIU Nan-nan, PENG Yong-chao, FU Xiu-hua, BAI Yue-jie, YANG Lu-yan, DONG Suo-tao, JIA Feng. Development of an anti–reflection coating for optical windows in multimode electro–optical detection systems[J]. *Chinese Optics*, In press. doi: 10.3724/CO.EN–2026–0012
惠冰, 刘楠楠, 彭永超, 付秀华, 白洁, 杨璐妍, 董所涛, 贾凤. 多模光电探测系统共光路窗口薄膜的研制[J]. 中国光学, 优先发表. doi: 10.3724/CO.EN–2026–0012

View online: https://doi.org/10.3724/CO.EN–2026–0012

文章编号　2097-1842(xxxx)x-0001-13

Development of an anti-reflection coating for optical windows in multimode electro-optical detection systems

HUI Bing[1 *], LIU Nan-nan[1], PENG Yong-chao[1], FU Xiu-hua[2], BAI Yue-jie[1], YANG Lu-yan[1], DONG Suo-tao[3], JIA Feng[1]

(1. *North Navigation Control Technology Co.Ltd.*, *Beijing* 100176, *China*;

2. *Changchun Univ Sci* & *Technol*, *Sch Optoelect Engn*, *Changchun* 130013, *Peoples R China*;

3. *Changchun Univ Sci* & *Technol*, *Zhongshan Inst*, *Zhongshan* 528437, *Peoples R China*)

* *Corresponding author*, *E-mail*: *hb_optical*@126.*com*

Abstract: As a critical component of integrated optoelectronic detection systems, multispectral ZnS windows enable multiband, common-path optical configurations. In this study, a broadband anti-reflection coating was designed and fabricated on multispectral ZnS substrates for multimodal detection applications covering the visible spectrum, the 905 nm laser band, and the long-wave infrared (LWIR) region. The residual stress, deposition process, coating design, and error sources of single-layer YbF_3 films were systematically investigated. By examining the effects of ion-source parameters on the stress of YbF_3 films, the optimal deposition conditions were determined to be a bias voltage of 150 V and a discharge current of 50 A. Initial experiments showed that the average transmittance in the visible band was only 73.35%. Inverse analysis indicated that this deviation was mainly caused by a systematic error in the tooling factor. After correcting the tooling-factor deviation and implementing an optimized monitoring strategy based on inverse spectral analysis, the layer-thickness error was effectively reduced, enabling precise control of highly thickness-sensitive layers. Normalized-coordinate analysis further revealed pronounced wavelength-dependent differences in spectral sensitivity between the visible and infrared regions. Therefore, a targeted single-band optimization strategy, combined with segmented monitoring of highly sensitive layers, was adopted to compensate for spectral shifts induced by cumulative thickness errors during multilayer deposition. The measured results show that, within an incidence-angle range of 0-15°, the average transmittance reached 93.57% at 450-1 000 nm and 92.91% at 8 000-12 000 nm, satisfying the required performance specifications.

Key words: thin films; anti-reflection coating; multiband integration; multimode detection systems

收稿日期:2026-04-13; 修订日期:xxxx-xx-xx

基金项目:xxx

Supported by

多模光电探测系统共光路窗口薄膜的研制

惠　冰[1*], 刘楠楠[1], 彭永超[1], 付秀华[2], 白玥洁[1], 杨璐妍[1], 董所涛[3], 贾　凤[1]
（1. 北方导航控制技术股份有限公司, 北京 100176, 中国;
2. 长春理工大学 光电工程学院, 长春 130013, 中国;
3. 长春理工大学 中山研究院, 中山 528437, 中国）

摘要: 多光谱 ZnS 窗口作为复合光电探测系统的关键器件, 可实现多波段、共光路设计。本文以多光谱 ZnS 为基底, 设计并制备了适用于可见光、905 nm 激光及长波红外多模探测应用的宽波段减反膜。系统讨论了 YbF_3 单层膜的应力特性、制备工艺、膜系设计及误差分析, 通过研究不同离子源参数对 YbF_3 单层膜应力的影响, 分析并确定了制备的最佳参数为偏压 150 V, 放电电流 50 A。初步实验结果显示, 可见光波段的平均透过率仅为 73.35%, 逆向分析表明, 该偏差源于工具因子存在系统误差。通过修正工具因子偏差, 并结合基于逆向光谱分析优化的监控方案, 有效降低膜层厚度误差, 实现了对高灵敏度膜层厚度的精确控制。归一化坐标分析发现, 可见光与红外波段区间的光谱响应呈现显著的波长敏感度差异, 本文采用针对性的单波段优化策略, 并结合高灵敏度膜层的分段监控方法, 以补偿多层膜沉积过程中厚度累积误差所引起的光谱偏移。测试结果表明, 在 0~15°入射角范围内, 450~1 000 nm 波段平均透过率达到 93.57%, 8 000~12 000 nm 波段平均透过率达到 92.91%, 满足性能指标要求。

关　键　词: 薄膜; 减反膜; 多波段; 多模探测系统
中图分类号: O482.31　**文献标志码:** A　**doi:** 10.3724/CO.EN-2026-0012　**CSTR:** 32171.14.CO.EN-2026-0012

1 Introduction

With advances in multimode electro-optical detection technology, multimode detection systems increasingly require multispectral common-path architectures instead of conventional multi-path designs, thereby reducing system volume and weight for terminal-guidance applications [1].

Multimode detection technology requires the integration of three spectral channels for target-background detection, namely visible imaging operating at 450-800 nm, infrared imaging at 8 000-12 000 nm, and laser detection at 905 nm. The visible band enables direct optical imaging of the target, the laser band facilitates target detection, tracking, and ranging, and the infrared band guarantees clear imaging during nighttime and low-illumination scenarios, thereby enabling all-weather day-and-night operation. These modalities complement each other, enhancing target recognition performance and enabling all-weather operational capability.

The implementation of multispectral common-path optical systems critically relies on thin-film technology to ensure that each spectral band meets its performance requirements. Multiband infrared coating technology remains a major research focus in the field of optical thin films.

Substantial progress has been made for different spectral bands and substrate materials. In 2007, Fu Xiuhua et al. prepared 3-5 μm and 8-12 μm dual-band infrared anti-reflection coatings on ZnS domes via electron-beam and ion-assisted deposition[2]. In 2016, triple-band coatings covering visible, laser, and mid-wave infrared bands were realized on ZnSe substrates[3]. In 2019, high-transmittance films over 1.5-5 μm were fabricated on silicon substrates with transmittance above 96.54%[4]. Relevant research also summarized the development status of domestic integrated optical thin film technology for spectral imaging systems[5]. In 2021, Zhou et al. developed infrared dual-color filter films working at 3.2-3.8 μm and 4.9-5.4 μm bands to meet multispectral detection demands[6]. In 2022, Li et al. fabricated dual-band anti-reflection coatings applicable to 1 064 nm laser and long-wave infrared range with superior optical performance[7].

International studies have focused on innovative film structures, fabrication techniques, and multifunctional coatings. Novel multilayer designs integrate infrared optical performance with radiative cooling capability[8]. Laser-etching techniques have also been used to fabricate anti-reflection microstructures, which greatly enhance the optical transmittance and laser damage resistance of infrared elements[9]. These explorations offer new approaches to improving the performance of multiband thin films.

Although extensive research[10-15] has been conducted on anti-reflection coatings for the visible, near-infrared, and mid-wave infrared bands, few studies have addressed broadband multiband coatings that simultaneously cover the visible and long-wave infrared regions.

This study focuses on broadband transmittance enhancement from the visible to the far-infrared, covering the visible television band, the 905 nm laser band, and the long-wave infrared band. For specific performance requirements, the average transmittance in the 450-1 000 nm and 8 000-12 000 nm bands needs to surpass 90% when the incidence angle is between 0° and 15°. Few materials exhibit high transmittance across both the visible and mid-to-long-wave infrared regions simultaneously. Moreover, their refractive indices and extinction coefficients exhibit pronounced wavelength dependence across these spectral ranges, resulting in discrepancies between theoretical design and practical fabrication outcomes. In addition, the wide bandwidth requirement in the visible region and the large spectral separation between the two target bands result in complex multilayer structures consisting of a large number of thin films. Therefore, enhancing thickness control accuracy and reducing film stress represent key challenges in this work.

2 Thin-film materials and process investigation

2.1 Materials selection

According to the specified technical performance requirements, the selection of coating materials must ensure low absorption loss in both the visible and infrared spectral regions, sufficient mechanical strength, stress compatibility between adjacent film layers, and strong adhesion between the coating and the substrate[16]. In this study, multispectral zinc sulfide (ZnS) was adopted as the substrate material. ZnS exhibits a broad transmission window from 380 to 14,000 nm, and its spectral transmittance curve is presented in Fig. 1. Multispectral ZnS was selected as the high refractive index material in the coating system. Ytterbium fluoride (YbF_3), which offers good stress compatibility with ZnS, was chosen as the low refractive index material. YbF_3 exhibits high transmittance over 220-14 000 nm.

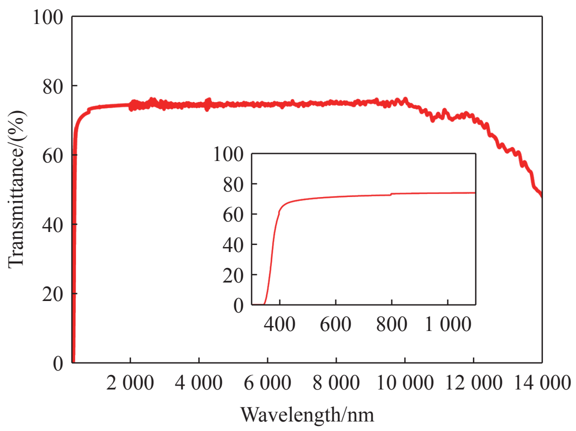

Fig. 1 Transmission spectrum curve of multispectral ZnS substrate.

2.2 Process investigation of single-layer YbF_3 films

Although YbF_3 demonstrates favorable mechanical strength and superior abrasion resistance relative to other fluoride-based materials, substantial internal stress may accumulate when the YbF_3 layer is deposited to a large thickness, potentially causing delamination and cracking. Three components make up film stress, namely surface stress, thermal stress and intrinsic stress. Surface stress is determined by the surface tension of the film layer and the interfacial tension between the film and the substrate. Thermal stress originates from the mismatch in thermal expansion coefficients between the coating and the substrate. Intrinsic stress, also referred to as internal stress, originates from the microstructural evolution during film growth. When the substrate, coating materials, and multilayer design are fixed, the overall stress is dominated by the intrinsic stress of the film layers[17-19].

When a thin film is deposited onto a substrate, the stress within the film induces deformation of the substrate surface profile. In this study, BK7 glass was adopted as the substrate material for single-layer YbF_3 experiments. Based on elastic mechanics theory[20-21], when the film thickness is much smaller than the substrate thickness, the film stress can be calculated using the Stoney formula[22] from the change in the substrate's peak-to-valley (PV) value before and after deposition. The film stress is given by

$$\sigma = \frac{E_s d_s^2}{6(1-v_s)d_f}\left(\frac{1}{R_f}-\frac{1}{R_s}\right) , \qquad (1)$$

where E_s is the Young's modulus of the substrate (82 GPa), v_s is the Poisson's ratio (0.17), R_f is the radius of curvature of the substrate after coating, and R_s is the radius of curvature before coating.

$$R_s = \frac{r^2}{2f_s\lambda} , \qquad (2)$$

$$R_f = \frac{r^2}{2f_f\lambda} . \qquad (3)$$

In these expressions, r denotes the measurement radius, f_s and f_f represent the PV values before and after coating, respectively, and λ is the wavelength of the interferometric laser used in the measurement.

During film deposition, plasma source parameters are among the critical factors that influence film stress[23-25]. Based on the above analysis, this study investigates the effects of different plasma source conditions on the intrinsic stress of YbF_3 thin films. Adjusting the ion-assisted deposition parameters to reduce film stress allowed us to determine the optimal deposition conditions and corresponding optical constants for the multilayer coating design.

The deposition process parameters used in the experiment are listed in Tab. 1.

Tab. 1 Deposition parameters for the control experiments.

Experiment	Vacuum (mbar)	Temperature (°C)	Rate ($nm\cdot s^{-1}$)	APS Discharge current (A)	APS Bias voltage (V)	Film thickness (nm)
A	5×10^{-6}	120	0.5	50	120/130/140/150/160	500
B	5×10^{-6}	120	0.5	40/45/50/55	150	500

The surface of coated substrates, 30 mm in diameter and 2 mm thick, was measured using a ZYGO laser interferometer. To mitigate diffraction-induced interference at the coating edge caused by the fixture, a 90% clear aperture of 27 mm in diameter was adopted during the measurement. When the ion source current was maintained at 50 A and the bias voltage was set to 120 V, 130 V, 140 V, 150 V, and 160 V, respectively, the corresponding results are shown in Fig. 2.

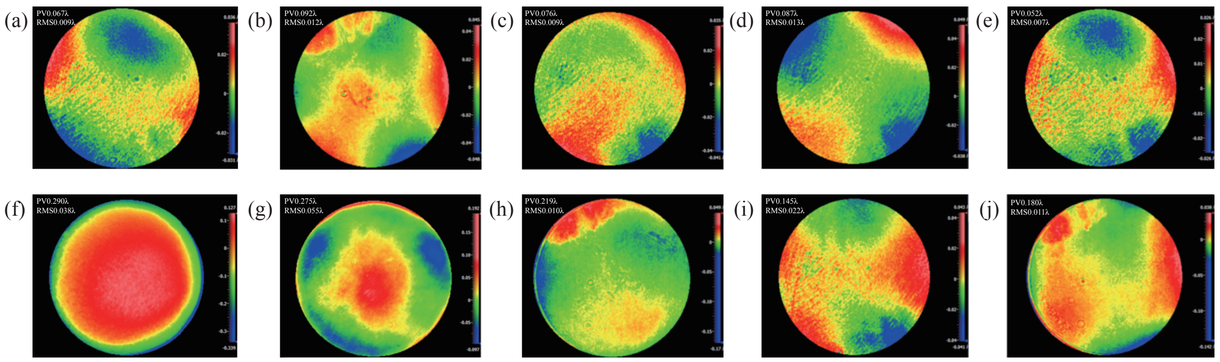

Fig. 2 Surface profiles of the substrate before coating and of YbF_3 films deposited under different ion-source bias voltages. (a)120 V; (b)130 V; (c)140 V; (d)150 V; (e)160 V; Surface measurement results of YbF_3 films under different ion source bias voltages. (f)120 V; (g)130 V; (h)140 V; (i)150 V; (j)160 V.

When the ion source bias voltage was set to 120 V, 130 V, 140 V, 150 V, and 160 V, the variations in the peak-to-valley (PV) values of the film surface were 0.290 λ, 0.183 λ, 0.143 λ, 0.058 λ, and 0.128 λ, respectively. The corresponding variation trend of film stress is shown in Fig. 3(a). As the ion source bias voltage increased, the stress of the YbF_3 thin film exhibited a trend of initially decreasing and then increasing. The minimum film stress was obtained at a bias voltage of 150 V.

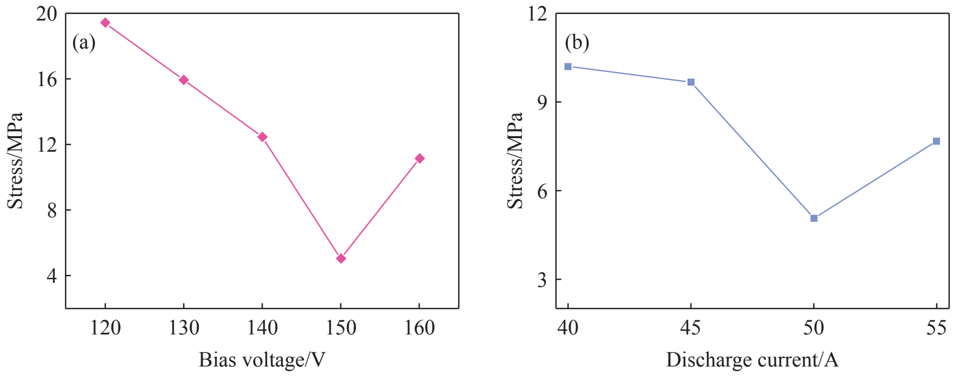

Fig. 3 (a) Variation of YbF_3 film stress under different ion source bias voltages; (b) Variation of YbF_3 film stress under different ion source discharge currents.

When the ion source discharge current was set to 40 A, 45 A, 50 A, and 55 A, the variations in the PV values of the film surface were 0.117 λ, 0.111 λ, 0.058 λ, and 0.088 λ, respectively. The corresponding surface measurement results are shown in Fig. 4, and the variation trend of film stress is presented in Fig. 3(b). As the ion source discharge current increased, the stress variation was relatively small, initially decreasing slightly before increasing, with a minimum at 50 A.

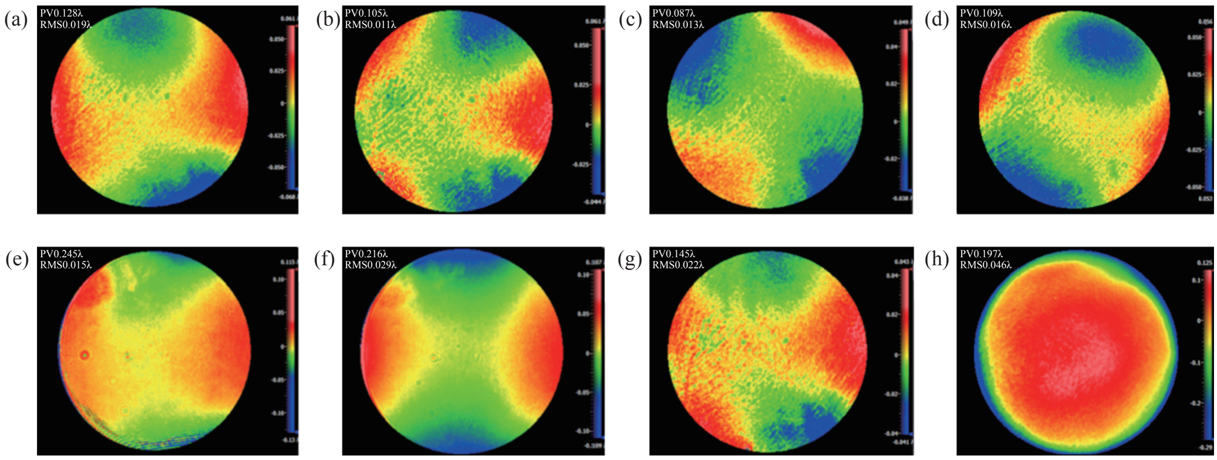

Fig. 4 Surface profile of the substrate before deposition (pre-experiment). (a)40 A; (b)45 A; (c)50 A; (d)55 A. Surface measurement results of YbF_3 films under different ion source discharge currents. (e)40 A; (f)45 A; (g)50 A; (h)55 A.

In summary, the stress variation of YbF_3 thin films is primarily influenced by the ion source bias voltage. As shown in Fig. 3(a), the film stress initially decreases and then increases with bias voltage, reaching a minimum at 150 V. In contrast, the discharge current has a weaker effect; the stress shows a slight decrease followed by an increase, with a minimum at 50 A. Considering the impact of film stress on practical application requirements, the final optimized deposition parameters were selected as a bias voltage of 150 V and a discharge current of 50 A.

In this study, the optical constants of ZnS and YbF_3 thin films were characterized under actual deposition conditions. The refractive indices in the 400-1 000 nm visible and near-infrared band were accurately measured using a J.A. Woollam M2000 spectroscopic ellipsometer. In contrast, the optical constants in the 8 000-12 000 nm long-wave infrared band were derived from numerical fitting of the experimental spectral data. The calibrated optical constant parameters of the two thin film materials are presented in Fig. 5.

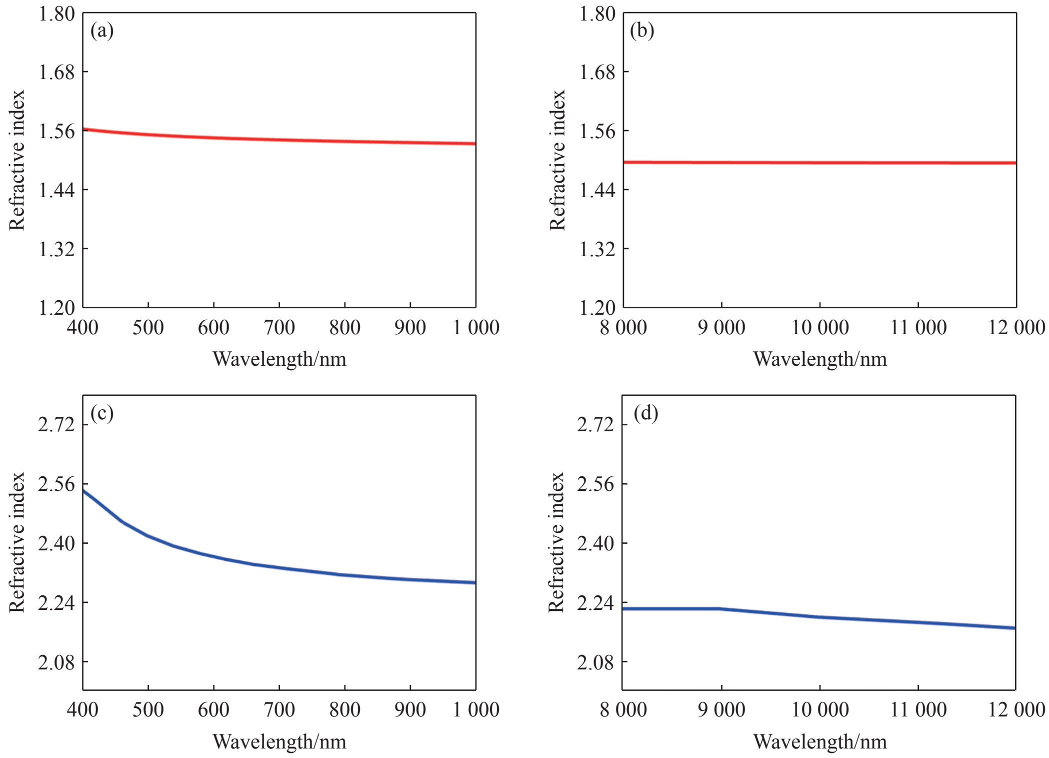

Fig. 5 Refractive-index dispersion curves of YbF_3 and ZnS. (a) Refractive index curve of YbF_3 for 400-1 000 nm; (b) Refractive index curve of YbF_3 for 8 000-12 000 nm; (c) Refractive index curve of ZnS for 400-1 000 nm; (d) Refractive index curve of ZnS for 8 000-12 000 nm.

3 Coating design and fabrication

3.1 Coating design

In this study, a dual-band high-transmittance coating covering the ranges of 450-1 000 nm and 8 000-12 000 nm was designed on a ZnS substrate. The specified incidence-angle range, broad visible-band bandwidth, and large separation between the visible and infrared bands make the coating design challenging. According to the conventional Baumeister theory of anti-reflection coating design[26], broadband design presents inherent limitations, necessitating more sophisticated optimization strategies. Based on thin-film optical theory, the optical admittance of a single-layer film can be expressed using the characteristic matrix method, as shown in Eq. (4).

$$Y_1 = \frac{C}{B} = \frac{\eta_2 \cos\delta_1 + i\eta_1 \cos\delta_1}{\cos\delta_1 + i(\frac{\eta_2}{\eta_1})\sin\delta_1} \quad , \qquad (4)$$

where $M = \begin{bmatrix} B \\ C \end{bmatrix} = \begin{bmatrix} \cos\delta_1 & \frac{i\sin\delta_1}{\eta_1} \\ i\eta_1\sin\delta_1 & \cos\delta_1 \end{bmatrix} \begin{bmatrix} 1 \\ \eta_2 \end{bmatrix}$ is the characteristic matrix of a single-layer film, $\delta_1 = \left(\frac{2\pi}{\lambda}\right) n_1 d_1 \cos\theta_1$, λ denotes the wavelength.

Following Baumeister's multilayer anti-reflection coating concept, the coating stack can be treated as an equivalent optical admittance. Accordingly, the overall characteristic matrix of the multilayer system is given by the product of the individual layer matrices, as expressed in Eq. (5).

$$M=\prod_{j=1}^{K}M_j\quad . \qquad (5)$$

The equivalent optical admittance of the multilayer system is then given by

$$Y=\frac{C}{B}\quad , \qquad (6)$$

where $\begin{bmatrix} B \\ C \end{bmatrix}=M\begin{bmatrix} 1 \\ n_s \end{bmatrix}$, n_s represents the refractive index of the substrate.

During coating design, a merit function was introduced, as defined in Eq. (7)

$$MeritFunction=\frac{1}{N}\sum\nolimits_{\lambda}\sum\nolimits_{\theta}W(\lambda,\theta)\left[T_{target}-T(\lambda,\theta)\right]^2\quad , \qquad (7)$$

where N is the total number of sampling points, λ denotes wavelength, θ represents the angle of incidence, and $T(\lambda,\theta)$ is the calculated transmittance of the current coating system at wavelength λ and incidence angle θ. The merit function incorporates a weighting function $W(\lambda,\theta)$ to emphasize optimization at spectral band edges and specified incidence angles, while reducing the weight assigned to other spectral regions.

To achieve optimal anti-reflection performance, the equivalent optical admittance of the multilayer system should be made as close as possible to the refractive index of air ($n_a=1$). Since the outermost layer forms the first film-air interface and determines the initial admittance transformation direction, YbF_3 was selected as the outermost layer[27].

According to the technical specifications, the initial coating structure was set as Sub | (HL)^15 | Air where Sub represents the multispectral ZnS substrate, H denotes a quarter-wave optical thickness layer of multispectral ZnS, L denotes a quarter-wave optical thickness layer of YbF_3, and the reference wavelength was set to 1 500 nm.

Thickness optimization was performed using OptiLayer, with wavelength and incidence angle targets specified in the optimization objectives. A combination of the gradient refinement algorithm and needle optimization algorithm was employed for global optimization. ZnS was adopted as the first interfacial layer to enhance the adhesion between the coating and the substrate. To reduce thickness errors associated with quartz crystal monitoring during deposition, a minimum physical thickness constraint of 10 nm was imposed.

The optimized theoretical spectral performance is shown in Fig. 6. The final coating structure consisted of 34 layers with a total physical thickness of 1.6 μm. At normal incidence (0°), the calculated double-sided average transmittance reached 99.02% over the range of 450-1 000 nm and 98.41% over the range of 8 000-12 000 nm.

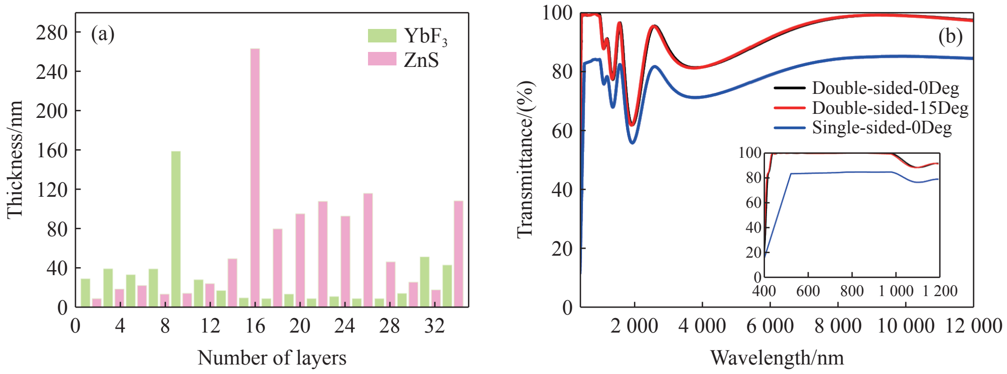

Fig. 6　Layer thickness distribution of the coating stack and theoretical spectral performance of the multispectral anti-reflection coating. (a) Thickness distribution map of the multilayer coating system; (b) Theoretical spectral curve of the multispectral anti-reflection film design.

3.2　Fabrication process

The coatings were fabricated by thermal evaporation using an ARES 1 100 vacuum coating system, manufactured by Bühler Leybold Optics, Germany. The system is equipped with an oil-free turbomolecular pumping system, an HPE16 electron-beam evaporator, a 12-position rotating resistive evaporation source, an APSpro ion source, and an INFICON IQM-6 six-channel quartz crystal thickness monitoring system. Both YbF_3 and ZnS layers were deposited by resistive thermal evaporation. The substrate temperature was maintained at 120 ± 3 °C during deposition. To enhance adhesion, the substrate was pre-treated with an ion beam prior to deposition.

In addition to the baseline deposition parameters listed in Tab. 2, a segmented thickness-control strategy was adopted during multilayer fabrication. Given the high spectral sensitivity of YbF_3 layers revealed by reverse analysis, the tooling factor of YbF_3 was calibrated separately from that of ZnS, and the outermost YbF_3 layer was monitored separately to reduce cumulative thickness deviation. This process adjustment was introduced to improve visible-band spectral stability while maintaining the infrared-band transmittance.

Tab. 2 Deposition process parameters.

Material	Deposition temperature (°C)	Rate ($nm \cdot s^{-1}$)	APS Parameters	Tooling
ZnS	120	0.8	-	77.5
YbF_3		0.5	140 V/50 A	70.6

3.3 Testing and analysis

The transmittance over the 450-1 000 nm spectral range was measured using a Cary 5 000 UV-Vis-NIR spectrophotometer (Agilent Technologies), whereas the transmittance in the 8 000-12 000 nm range was measured using a Spectrum 3 Optica Fourier transform infrared (FTIR) spectrometer (PerkinElmer). The single-sided transmittance spectra measured at normal incidence (0°) are shown in Fig. 7(a) and Fig. 7(b).

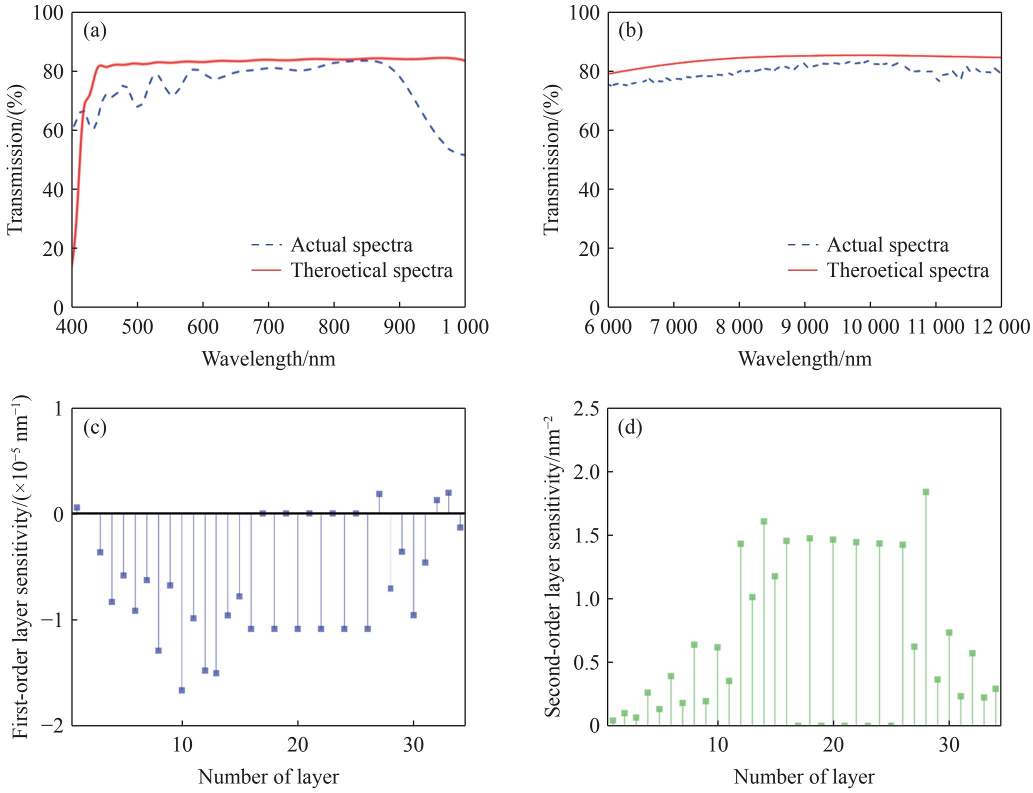

Fig. 7 Measured single-sided transmittance spectra of the coating and first-order and second-order sensitivity of the coating stack. (a) Transmission test spectral curve for 400-1 000 nm; (b) Transmission test spectral curve for 8 000-12 000 nm; (c) First-order sensitivity; (d) Second-order sensitivity.

The measured average transmittance over the 450-1 000 nm band was 73.35%, notably below the theoretical design target of 82.52%. Pronounced transmittance ripples were also observed in the 450-640 nm spectral region. Compared with the theoretically designed visible transmission bandwidth, the measured bandwidth was noticeably narrower. For the 8 000-12 000 nm band, the measured average transmittance was 82.76%, in good agreement with the theoretical value of 84.73%.

The significant deviation observed between the measured and theoretical transmittance curves in the visible region cannot be attributed solely to absorption by the substrate and coating materials within this spectral range. The discrepancies between actual and theoretical layer thicknesses must also be analyzed. Fig. 7(c) and 7(d) show the first-order and second-order sensitivity analyses of the coating stack.

The first- and second-order sensitivity distributions of the coating stack show that YbF_3 layers have relatively high overall sensitivity and dominate the spectral performance determination of the optical system. Inverse analysis attributed the narrowing of the visible-band transmission bandwidth primarily to a systematic deviation in the tooling factor during YbF_3 deposition, which resulted in an actual deposited thickness of only 92.42% of the theoretical value. This thickness deviation propagates through the coating stack, resulting in contraction of the visible transmission bandwidth.

Let the theoretical physical thickness of the j YbF_3 layer be d_{j0}. Owing to the systematic error of the quartz crystal microbalance (QCM), which is represented by the tooling factor k, and assuming that k remains constant during the deposition of the YbF_3 film, the actual physical thickness d_j can be expressed as

$$d_j = kd_{j0} \quad , \tag{8}$$

where n_{j0} denotes the refractive index of the YbF_3 thin film. When the dispersion relation is neglected, n_{j0} can be approximately regarded as a constant within the considered wavelength range and is independent of the film thickness. The theoretical phase thickness of a single layer is $\delta(\lambda)_{j0} = \left(\frac{2\pi}{\lambda}\right) n_{j0} d_{j0}$, and the corresponding actual phase thickness $\delta(\lambda)_j$ is

$$\delta(\lambda)_j = \left(\frac{2\pi}{\lambda}\right) n_{j0} d_j = \left(\frac{2\pi}{\lambda}\right) n_{j0} \cdot (kd_{j0}) = k\delta(\lambda)_{j0} \quad . \tag{9}$$

Substituting Eq. (9) into the characteristic matrix M and Eq. (5), the total characteristic matrix of the multilayer coating system can be written as

$$M_j = \prod_{j=1}^{K} M_{j0(\mathrm{k})} \quad . \tag{10}$$

At the central wavelength λ_0, the theoretically designed phase thickness is $\delta_{j0}(\lambda_0)$. Without re-optimizing the coating system, this value is usually an integer multiple of $\frac{\pi}{2}$. For any wavelength λ, the phase thickness can be expanded as

$$\delta_{j0}(\lambda) = \left(\frac{2\pi}{\lambda}\right) n_{j0} d_{j0} = \frac{\lambda_0}{\lambda} \delta_{j0}(\lambda_0) \quad , \tag{11}$$

where $g = \frac{\lambda_0}{\lambda}$ is defined as the relative wavenumber, also referred to as the normalized frequency. Therefore, Eq. (11) can be simplified as

$$\delta_{j0}(\lambda) = g\delta_{j0}(\lambda_0) \quad . \tag{12}$$

For an actually deposited film, the tooling factor can be equivalently expressed in the normalized-frequency domain, and the phase thickness becomes

$$\delta_j(\mathrm{g}) = k\delta_{j0}(\mathrm{g}) = k \cdot \mathrm{g}\delta_{j0}(\lambda_0) \quad . \tag{13}$$

The above analysis indicates that the actual phase thickness is equivalent to multiplying the theoretical phase thickness by the constant k, or equivalently replacing the normalized frequency g with $k \cdot \mathrm{g}$. Therefore, in the normalized-frequency domain, the actual spectral response can be approximately represented as a scaling transformation of the theoretical spectral-response function. In other words, the overall spectral response can be approximated as a linear scaling along the wavelength axis, and the relative spectral shift becomes a constant that is independent of wavelength.

For the infrared band, if a fixed proportional systematic deviation exists in the physical thickness, the multilayer stack can be approximated as a uniformly scaled structure. However, in the normalized frequency coordinate system, the spectral response of the optical thin films exhibits approximate scale invariance. Therefore, the difference between the theoretical design and the measured spectrum is determined solely by deviations in the tooling factor and is independent of the absolute wavelength. This indicates that the infrared band is relatively insensitive to proportional deviations in the deposition thickness. The bandwidth variation caused by a systematic tooling factor deviation is effectively suppressed at longer wavelengths, leading to a smaller discrepancy between the measured and theoretical infrared spectra.

Consequently, the coating stack can be optimized by comparing the measured and theoretical spectra in the visible region, without explicitly re-optimizing the infrared band. The narrowing observed in the visible transmission bandwidth can be ascribed to the systematic tooling factor deviation of the YbF_3 layers. When the scaling coefficient is 0.92, a noticeable reduction in the visible bandwidth can be observed. Further reverse analysis indicates that the pronounced spectral oscillations in the 450-640 nm region originate from the thickness deviation of the outermost YbF_3 layer. A comparison between the experimental results and the fitted analysis is presented in Fig. 8.

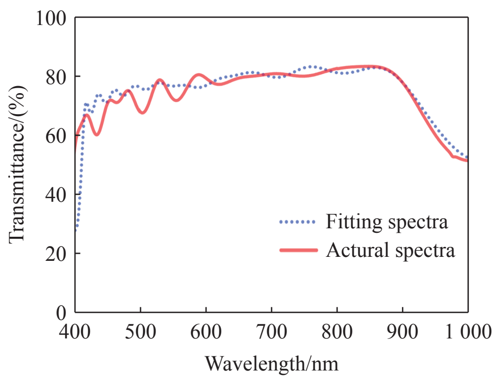

Fig. 8 Comparison between the fitted spectrum and the measured spectral curve.

The entire deposition process was monitored using a quartz crystal microbalance (QCM). This technique controls the film thickness by monitoring the variation in the oscillation frequency of an AT-cut quartz crystal. As the film thickness increases, the oscillation frequency decreases, reducing detection sensitivity and introducing monitoring errors[28].

Theoretical and experimental analyses confirmed that adjusting the tooling factor for YbF_3 layers and independently monitoring the outermost layer significantly improve spectral performance.

Specifically, optimization prioritized layers with higher first- and second-order sensitivity in the visible band rather than globally re-tuning the entire stack. This sensitivity-prioritized correction strategy reduced error propagation from the outer YbF_3 layers toward the inner multilayer stack and was more effective than uniform thickness compensation. As a result, the visible-band ripple was suppressed and the measured spectrum became more consistent with the theoretical profile, while the infrared band remained comparatively stable because of its lower sensitivity to proportional thickness deviation. These modifications effectively smoothed the overall spectral response and suppressed the oscillations in the visible band. The adjusted measured spectral curves are presented in Fig. 9.

Within an incidence angle range of 0°-15°, the average transmittance reached 93.57% in the 450-1 000 nm region and 92.91% in the 8 000-12,000 nm region, thus meeting the specified requirements.

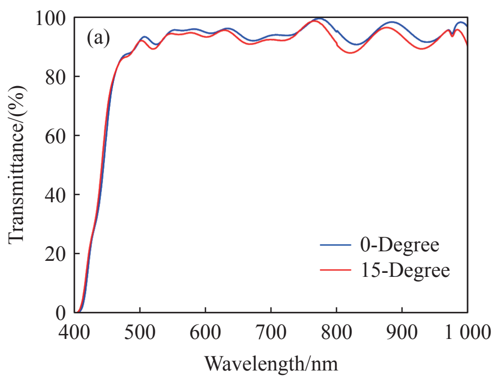

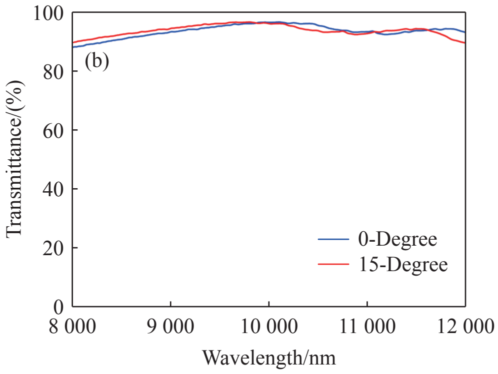

Fig. 9 Measured spectral transmittance curves. (a) 0-15° transmittance spectrum over 450-1 000 nm;(b) 0-15° transmittance spectrum over 8 000-12 000 nm.

3.4 Environmental testing

To ensure product reliability under operational conditions, the following environmental tests were conducted on the samples.

(1) Adhesion test

At room temperature, a 3M adhesive tape with a width of 2 cm and a peel strength of no less than 2.74 N/cm was firmly applied to the coated surface within the effective clear aperture. Care was taken to ensure that the tape was flat and free of air bubbles, and was then rapidly peeled off in a direction perpendicular to the surface. No film delamination or cracking was observed on the sample surface.

(2) Temperature and thermal shock test

The samples were placed at a low temperature of −46 ± 2 °C and a high temperature of 71 ± 2 °C, with a holding time of 2 h under each temperature condition. The chamber temperature ramp rate did not exceed 2 °C/min. After cooling back to room temperature, the coating surface was carefully examined, and no defects such as peeling, delamination, cracking, or blistering were observed.

For the thermal shock test, the samples were alternately exposed to -46 ± 2 °C and 71 ± 2 °C. No peeling, delamination, cracking, or blistering was observed on the coating surface.

(3) Damp heat test

The samples were placed in a humidity chamber at a temperature of 50 ± 2 °C and a relative humidity of 95% to 100% for 24 hours. After removal from the chamber, the coating surfaces were inspected, and no peeling, delamination, cracking, or blistering defects were detected.

After the aforementioned environmental tests, no significant changes were observed in the spectral performance of the samples. The fabricated visible, laser, and LWIR anti-reflection coating exhibited excellent environmental stability and satisfied the requirements for practical applications.

4 Conclusion

On the basis of the material optical properties and design requirements, multispectral ZnS and YbF_3 were selected as high and low refractive index materials, respectively. The influence of different ion source process parameters on film stress was investigated, and the optimal ion source parameters for YbF_3 deposition were determined. Using the calculated material parameters, the anti-reflection coating was designed and successfully fabricated via resistive thermal evaporation. Comparing experimental results with sensitivity distribution analysis and reverse simulation revealed the wavelength-dependent error sensitivity in different spectral bands. Targeted process optimization and precise monitoring of high-sensitivity layers were carried out accordingly. Ultimately, an anti-reflection coating applicable to visible, laser, and long-wave infrared multimode detection systems was successfully fabricated. Environmental tests confirm that the multiband anti-reflection coating exhibits stable performance and strong environmental adaptability. These results demonstrate the feasibility of broadband visible-laser-LWIR anti-reflection coating design for integrated multimode detection systems.

References:

[1] XIN Y W, PENG Y CH, ZHANG Y X, *et al*.. Investigation of 980/1550 nm dual-bandpass wide-cutoff filter in laser

communication system[J]. *Infrared Physics & Technology*, 2025, 150: 105945.

[2] 付秀华, 姜会林, 付新华, 等. 多波段红外增透与保护膜技术的研究[J]. 兵工学报, 2007, 28(10): 1183-1185.
FU X H, JIANG H L, FU X H, *et al*.. Study on multi-waveband infrared antireflection and protection film[J]. *Acta Armamentarii*, 2007, 28(10): 1183-1185. (in Chinese).

[3] 米高园, 张建付, 韩俊, 等. 电视、激光、中波红外多波段增透膜研究[J]. 激光与红外, 2016, 46(5): 593-596.
MI G Y, ZHANG J F, HAN J, *et al*.. Research on antireflection coating for TV, laser, mid-infrared wavebands[J]. *Laser & Infrared*, 2016, 46(5): 593-596. (in Chinese).

[4] 付秀华, 张功, 张静, 等. 短中波红外探测系统宽波段高透过率薄膜[J]. 红外与激光工程, 2019, 48(10): 101700.
FU X H, ZHANG G, ZHANG J, *et al*.. Short-medium infrared detection system broadband high transmittance film[J]. *Infrared and Laser Engineering*, 2019, 48(10): 101700. (in Chinese).

[5] 王多书, 李得天, 范栋, 等. 空间光谱成像及集成光学薄膜技术发展现状[J]. 真空与低温, 2019, 25(5): 285-294.
WANG D SH, LI D T, FAN D, *et al*.. Development status of space spectral imaging and integrated optical thin film technology[J]. *Vacuum and Cryogenics*, 2019, 25(5): 285-294. (in Chinese).

[6] 周晟, 王凯旋, 刘定权, 等. 3.2~3.8 μm 和 4.9~5.4 μm 红外双色滤光片的研制[J]. 中国光学, 2021, 14(3): 536-543.
ZHOU SH, WANG K X, LIU D Q, *et al*.. Research on infrared dual-color filters with 3.2~3.8 μm and 4.9~5.4 μm bands[J]. *Chinese Optics*, 2021, 14(3): 536-543. (in Chinese).

[7] 李子杨, 刘华松, 孙鹏, 等. 激光/长波红外双谱段减反射薄膜设计与制备[J]. 红外与激光工程, 2022, 51(3): 202109.
LI Z Y, LIU H S, SUN P, *et al*.. Design and preparation of laser/long-wave infrared dual-band antireflection thin film[J]. *Infrared and Laser Engineering*, 2022, 51(3): 202109. (in Chinese).

[8] WANG L, ZHANG SH Y, DONG J, *et al*.. Multi-band infrared camouflage compatible with radiative cooling and visible colors via a simple multilayer film structure[J]. *Optical Materials Express*, 2023, 13(10): 2746-2758.

[9] TESLENKO A, KONSTANTINOVA T, BUSHUNOV A, *et al*.. Antireflection microstructures on ZnSe for mid- and far-IR fabricated by femtosecond laser ablation assisted with wet chemical etching[J]. *Scientific Reports*, 2024, 14(1): 10743.

[10] SHAVEISI M, ALIPARAST P. Design and modeling of high-performance mid-wave infrared InAsSb-based nBn photodetector using barrier band engineering approaches[J]. *Frontiers of Optoelectronics*, 2023, 16(1): 5.

[11] MALM H, GAMFELDT A, VON WÜRTEMBERG R M, *et al*.. High image quality type-II superlattice detector for 3.3 μm detection of volatile organic compounds[J]. *Infrared Physics & Technology*, 2015, 70: 34-39.

[12] PENG Y CH, HUI B, XIN Y W, *et al*.. Investigation into wide-angle bandpass filter for UV fluorescence imaging system[J]. *Journal of Materials Science*, 2025, 60(1): 339-354.

[13] ZHU Y, LIU CH CH, SUN P, *et al*.. Ultrathin, polishing-free diamond anti-reflective films for mid-wave infrared (MWIR) windows promoted by electrostatic spin-coating seeding[J]. *Applied Surface Science*, 2026, 722: 165554.

[14] CIANCI E, COPPA A, FOGLIETTI V. Young's modulus and residual stress of DF PECVD silicon nitride for MEMS free-standing membranes[J]. *Microelectronic Engineering*, 2007, 84(5-8): 1296-1299.

[15] ZHANG Q Y, LI X L, SHEN J, *et al*.. ZrO_2 thin films and ZrO_2/SiO_2 optical reflection filters deposited by sol-gel method[J]. *Materials Letters*, 2000, 45(6): 311-314.

[16] JENSEN T R, WARREN J, JOHNSON R L. Ion-assisted deposition of moisture-stable hafnium oxide films for ultraviolet applications[J]. *Applied Optics*, 2002, 41(16): 3205-3210.

[17] SAFIN R G, GAĬNUTDINOV I S, SABIROV R S, *et al*.. Solar-blind filter for the ultraviolet region[J]. *Journal of Optical Technology*, 2007, 74(3): 208-210.

[18] HITOSHI U. On-beam-assisted deposition of hard cBN films and internal stress relaxation by laminated layer[J]. *Kaken*, 2018, 1800123. **(查阅网上资料, 未能确认文献类型, 请确认文献类型及格式是否正确)**.

[19] MUKAI K, HUJITA S, TAKAYAMA S. Change of an internal stress exerted on each layer in AZO/Cu/Mo multilayered films on annealing[J]. *Journal of the Electrochemical Society*, 2022, 169(12): 122502.

[20] ZHANG SH, LIU B, ZHANG X, *et al*.. Reduction of internal stress in InGaZnO (IGZO) thin film transistors by ultra-thin metal oxide layer[J]. *Materials Science in Semiconductor Processing*, 2024, 173: 108093.

[21] ZHU H, JIANG H Y, GUO K, *et al*.. Development of wide-angle depolarizing reflector at 1064 nm[J]. *Materials*, 2023, 16(12): 4258.

[22] HONG I S, HWANG Y S, LEE G H, *et al*.. Ion-beam characteristics of novel helicon ion sources for different plasma

parameters[J]. *Review of Scientific Instruments*, 2000, 71(3): 1385-1388.

[23] KLIMOV A, BAKEEV I, OKS E, *et al*.. Forevacuum plasma source of continuous electron beam[J]. *Laser and Particle Beams*, 2019, 37(2): 203-208.

[24] ÖZHAN A E S, HACALOĞLU T, KAFTANOĞLU B. Development of hard, anti-reflective coating for mid wave infrared region[J]. *Infrared Physics & Technology*, 2021, 119: 103910.

[25] SAID S A M, AL-AQEELI N, WALWIL H M. The potential of using textured and anti-reflective coated glasses in minimizing dust fouling[J]. *Solar Energy*, 2015, 113: 295-302.

[26] 付秀华, 张于帅, 寇洋, 等. 自由空间激光通信系统中多通道滤光膜的研制[J]. 中国激光, 2015, 42(4): 0407001.
FU X H, ZHANG Y SH, KOU Y, *et al*.. Study and fabrication of multi-channel filter film in free-space laser communication system[J]. *Chinese Journal of Lasers*, 2015, 42(4): 0407001. (in Chinese).

[27] 熊仕富, 付秀华, 刘冬梅, 等. 基于甲烷气体红外吸收特性窄带滤波器的研究[J]. 光子学报, 2017, 46(10): 1023003.
XIONG SH F, FU X H, LIU D M, *et al*.. Narrow-band filter based on infrared absorption characteristics of methane gas[J]. *Acta Photonica Sinica*, 2017, 46(10): 1023003. (in Chinese).

[28] CAO X Y, ZHANG Y X, WANG B, *et al*.. Integrated symmetric equivalent layer design and stress compensation for high-performance infrared dual-band depolarizing beam splitters[J]. *Infrared Physics & Technology*, 2026, 155: 106460.

Author Biography:

HUI Bing (1994—), female, born in Changchun, Jilin Province. She is a technician at North Navigation Control Technology Co., Ltd. She graduated from Changchun University of Science and Technology in 2018 with a Master's degree in Optical Engineering. Her main research direction is the development and performance evaluation of precision optical thin films. E-mail: hb_optical@126.com